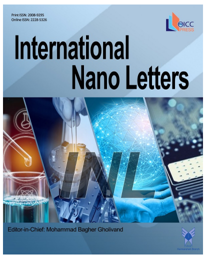


Volume 14, Issue 4, 142416 (1-10)

International Nano Letters (INL)

https://doi.org/10.57647/inl.2024.1404.16

# Enhancing Hyperthermic Oncology: A Computational Approach to Optimize $Fe_3O_4$@Au core-shell Configurations for Targeted Tumor Therapy

Somayeh Salmani[1,2,*], Somayeh Rahbari[1], Fereshteh Shafiepour[3]

[1] *Nanophysics Lab, Faculty of Physics, Kharazmi University, Tehran, Iran.*
[2] *Applied Sciences Research Center, Kharazmi University, Tehran, Iran.*
[3] *Physics Department, Purdue University, Indiana, U.S.*

[*] **Corresponding author:** salmani@khu.ac.ir



**Original Research**

**Abstract:**

This work focuses on Near- Infrared region and an incident laser with a wavelength of 808 nm to study the numerical optimization of the Fe3O4@Au core-shell nanostructure for enhanced hyperthermia treatment, specifically targeting skin cancer. Utilizing the simulation capabilities of COMSOL Multiphysics, we meticulously computed the optical properties-absorption, scattering, and extinction coefficients-of these nanostructures across varying incident wavelengths and core-to-shell ratios. Our findings reveal a pivotal dependency of maximum absorption rates on both the core-to-shell ratio and the parameters of the incident laser, marking a significant stride in the customization of hyperthermia therapy. Crucially, the study harnesses local temperature elevation as a therapeutic index for skin cancer treatment. The thermal mapping achieved delineates a stark contrast between the peak temperature of 56 °C within the tumor and a controlled 37 °C in the surrounding healthy tissue, showcasing the potential for targeted thermal ablation with minimal collateral damage. The graphical representations not only corroborate the theoretical model but also serve as a beacon for future clinical applications, promising a new horizon in the minimally invasive treatment of cancer with the utmost precision and minimal undesired effects.

**Keywords:**

Core-Shell structure; Hyperthermia; $Fe_3O_4$@Au; COMSOL multiphysics; Local temperature; Absorption cross-section

**Cite this article:** Salmani, S., Rahbari, S., Shafiepour, F. Enhancing Hyperthermic Oncology: A Computational Approach to Optimize $Fe_3O_4$@Au core-shell Configurations for Targeted Tumor Therapy. *Int. Nano Lett.* **14**(4), 142416 (2024).

## 1. Introduction

Plasmonic core-shell nanoparticles, known for their exceptional optical and thermal properties, have garnered significant attention as contrast agents in biomedicine [1–4] and Cancer treatment [5–7]. These metal nanoparticles (MNPs) interact strongly with incident electromagnetic fields, resulting in unique optical behavior [8]. Collective electron oscillations within the nanoparticles lead to localized surface plasmon resonance (LSPR) effects, enhancing the absorption and scattering of electromagnetic waves [9–13]. Geometric variations in MNPs cause shifts in their optical properties, spanning from visible to near-infrared wavelengths. To create an ideal nanomaterial for deep light penetration into human tissue, optimizing energy absorption within the optical window is crucial [14, 15].

Hyperthermia, a well-studied treatment method, has captured the interest of numerous researchers. Often employed alongside chemotherapy or radiation treatment [16–18], hyperthermia involves locally or systemically raising the tumor temperature to a range of 42 °C to 48 °C. Local hyperthermia, known for its minimal side effects, is commonly combined with other therapeutic approaches. Recent years have witnessed extensive investigations into nanoparticle structures for hyperthermia applications. Researchers have conducted both experimental and theoretical studies on spherical nanoparticles such as Au and Ag [19, 20]. These nanoparticles exhibit favorable optical and electrical properties, making them valuable for bio-imaging, biosensors, and photo-thermal treatments [21, 22]. Their functionalization with ligands, antibodies, or pharmacological molecules enhances their applicability for active or passive drug delivery. Notably, $Fe_3O_4$@Au nanoparticles have gained widespread attention due to their diverse biological applications [23–28]. Ongoing research focuses on plasmonic advancements, particularly the near-field enhancement of core-shell dimer nanostructures.

An essential consideration in hyperthermia research involves the interaction between nanoparticles and laser light at the nanoscale. Analyzing the absorption spectrum of nanomaterials in the visible region is a widely used strategy to understand this interaction. Scattering, absorption, and extinction coefficients provide crucial information about the interplay between light and nanoparticles [29].

In this study, we numerically investigate the optical properties of $Fe_3O_4$@Au core-shell nanoparticles using COMSOL Multiphysics (Finite Element Model). Initially, we calculate the optical properties by varying the shell thickness while maintaining a constant outer radius, focusing on absorption, scattering, and extinction coefficients. Subsequently, we apply the optimized $Fe_3O_4$@Au core-shell structure to analyze the thermal distribution function in skin cancer, which we discuss in the following sections.

## 2. Numerical method

### 2.1 RF module

As stated, at first, numerical investigation of the optical properties of Magneto-plasmonic nanostructures have been used by the finite element method (FEM), and the absorption, scattering, and extinction coefficients were calculated. Within this specific module, Maxwell's equations are formulated as a wave equation governing the electric field, as referenced in [30, 31]:

$$\nabla \times \mu_r^{-1}(\nabla \times E) - k_0^2 \varepsilon E = 0 \tag{1}$$

where $\mu_r$ denotes the relative permeability of the material in question, $E$ represents the electric field, $k_0$ is the wave propagation vector, and $\varepsilon$ signifies the dielectric permittivity of the material, encompassing both its real and imaginary components. The displacement field model employed herein is predicated upon the refractive index of the material.

Within the COMSOL simulation environment, electromagnetic waves can be resolved through two distinct formulations: The Full Field and the Scattered Field approaches. The Full Field formulation necessitates the specification of an input port, direction, and location for the input field. However, given that our module operates within an infinite domain, the Scattered Field formulation was adopted, wherein the input field is applied across the entire simulation domain. Consequently, a plane wave, polarized along the $x$-axis and advancing along the z-axis, is established as per reference [31]:

$$E_b = E_0\, e^{(-j\frac{2\pi n}{\lambda}z)\hat{i}} \tag{2}$$

With $E_0$ being the amplitude of the wave (1 V/m), $n$ the refractive index of the medium (in case, skin, $n = 1.4$), and $\lambda$ the wavelength ($400 - 1100$ nm in our study).

To mitigate the boundary reflections within the computational domain, a perfectly matched layer (PML) was constructed encircling the physical domain-comprising both the nanoparticle and its immediate environment-with a thickness of $\lambda_{\max}/2$. Additionally, a scattering boundary condition was applied to the domain's periphery, ensuring that waves impinging upon the computational boundary do not reflect back into the central domain of interest [32]. Due to using a symmetric geometry, a perfect electric conductor and a perfect magnetic conductor were applied.

The geometrical parameters that measure the absorption, scattering, and extinction properties of a material are known as the absorption cross-section, scattering cross-section, and extinction cross-section, respectively. These parameters are mathematically defined in references [31, 32]:

$$\begin{aligned} \sigma_{abs}[\mathrm{m}^2] &= 4 \times \frac{W_{abs}\,[\mathrm{W}]}{S_I\,[\frac{\mathrm{W}}{\mathrm{m}^2}]} \\ \sigma_{sca} &= 4 \times \frac{W_{sca}}{S_I} \\ \sigma_{ext} &= \sigma_{abs} + \sigma_{sca} \end{aligned} \tag{3}$$

where $W_{abs}$ and $W_{sca}$ are the energies absorbed and scattered by the nanoparticle, respectively, and $S_I$ is the intensity of input light (power per unit area). The operation was multiple 4 to calculate the result in the whole geometry.

$$S_I = \frac{1}{2} c \varepsilon_0 |E_0|^2 \hat{k} \tag{4}$$

In the equations presented $c$ represents the speed of light in vacuum and $\varepsilon_0$ stands for the vacuum permittivity, respectively. The symbol $\hat{k}$ indicates the direction of propagation of the incoming light wave.

The numerical solution provides the values for the power absorbed and scattered as delineated in Eq. (3) [30]:

$$W_{abs} = \frac{1}{2} \int \int \int_v \mathrm{Re}[(\sigma E + j\omega D)E^* + j\omega B H^*] dV \tag{5}$$

$$W_{sca} = \frac{1}{2} \int \int \int_s \mathrm{Re}[E_{sca} \times H_{sca}^*] n dS \tag{6}$$

In the aforementioned expressions, $D$ signifies the displacement currents signifies the displacement currents $*$ represents the complex conjugate, respectively. In Eq. (5), the integration is throughout the volume of the nanoparticle, and in Eq. (6), the surface integral is over the surface of the nanoparticle.

The energy absorption by the nanoparticles can be efficiently determined within COMSOL by performing an integration of the power dissipation density across the nanoparticle's volume [31]:

$$W_{abs} = \int \int \int_{\Omega} Q_h d\Omega \tag{7}$$

In the context of this study, $Q_h$ is designated as the variable within COMSOL that quantifies the power dissipation density. Owing to its wavelength ($\lambda$) dependency, a parametric analysis was conducted across a spectrum of $\lambda$ values to ascertain the optical cross-section spectra. Furthermore, the quantification of the energy dispersed by the nanoparticles is accomplished in COMSOL through the integration of the Poynting vector across the nanoparticle's surface.

### 2.2 Bioheat transfer module

After that, the heat transfer in a tissue when a $Fe_3O_4$@Au core-shell nanostructure is placed in the tumor was utilized under an incident laser in 808 nm wavelength. The first continuous model was introduced in 1948 by Thomas Pennes to investigate heat transfer in human arm tissue. The Pennes equation is expressed as follows [33]:

$$\rho_t C_t \frac{\partial T_t}{\partial t} = \nabla(k\nabla T_t) + W_b \rho_b C_b (T_a - T_t) + q_m \qquad (8)$$

where $k$ is the thermal conductivity [W/(m·K)], $\rho$ is the tissue density [kg/m$^3$] and $C$ is the specific heat capacity in tissue [J/(kg·K)]. In the above equation, the $b$ shows the blood and $t$ is tissue. The $q_m$ is the amount of heat produced by the body's metabolism [W/m$^3$], $T_a$ is the arterial blood temperature [K] and $W_b$ is blood perfusion rate [m$^3$/(s·kg)]. Pennes's heat transfer equation is based on the thermal balance of blood and tissue, in such a way that blood enters the tissue with the temperature of the artery $T_b$ according to the coefficient of blood penetration rate, and after reaching the thermal equilibrium with the tissue, it leaves through the veins. Therefore, in this modeling, the rate of blood penetration through veins or capillaries in the tissue is uniform and isotropic. Also, there is a thermal balance between blood and tissue in the capillary structure of biological tissue.

## 3. Results and discussion

Our simulations aim to identify an effective hyperthermia treatment method for selectively destroying cancerous gland tissue while minimizing the impact on healthy tissue. Key factors include temperature distribution, maximum temperature achieved, stable state time, and tumor tissue boundary heat flux. Optimizing parameters is crucial for achieving the desired temperature distribution. Additionally, we consider the equation of biological heat transfer coupled with electromagnetic fields to quantify nanoparticle absorption across a wide range of wavelengths.

When irradiating a field onto a desired spherical nanoparticle, an induction field emerges. This internal induction field leads to a single general polarization and, consequently, only one dipole mode in our calculations. In the Rayleigh approximation, where the field fully penetrates such small nanoparticles due to their dimensions relative to the depth of penetration, and considering purely electrostatic aspects, minimal radiation is detectable from the conduction electrons within the spherical metal nanoparticles. In this approximation, only dipole modes are observed, emphasizing that absorption processes dominate over scattering processes.

As the dimensions of nanoparticles increase, particularly when the radius of spherical nanoparticles grows, surface effects become prominent. These effects arise due to the particle size exceeding the depth of field penetration into the metal. Consequently, a heterogeneous distribution of free charges occurs on the nanoparticle's surface. This charge distribution leads to additional peaks in the scattering and absorption spectra of metal nanoparticles, including modes such as quadrupole and octupole. Researchers studying nanoparticle size variations carefully consider these cases to provide precise physical justifications for changes in nanoparticle dimensions.

To investigate the impact of core-shell size parameters on absorption, we initially consider a fixed core diameter of 5 nm and vary the shell thickness from 2 to 10 nm. Simulation results (Fig. 1a) reveal that when the core diameter remains at 5 nm, increasing the shell diameter leads to reduced absorption intensity and a redshift in the absorption spectrum. This shift indicates a decrease in the effective refractive index of nanoparticles with larger shell diameters. Notably, nanoparticles with a 2 nm shell exhibit an absorption peak around 550 nm (green light), which redshifts to approximately 700 nm. Additionally, the absorption cross-section area decreases by a factor of 10, reaching approximately 100 nm$^2$.

For optimal heat generation, laser light around 550 nm should be used. Further simulations explore core diameters in the range of 10 to 50 nm, revealing consistent redshift patterns and absorption cross-section reductions across all modes (Fig. 1b to 1f).

In our subsequent analysis, we examine the scattering cross-section based on simulation results (Fig. 2). When the core diameter of nanoparticles remains fixed at 5 nm, increasing the shell diameter from 2 to 10 nm leads to reduced scattering intensity and a redshift (toward longer wavelengths) in the scattering spectrum. This redshift indicates a decrease in the effective refractive index of nanoparticles as the shell diameter increases. Remarkably, the scattering peak exhibits similarities to the absorption state: nanoparticles with a 2 nm shell exhibit an absorption peak around 550 nm (green light), which redshifts to approximately 700 nm. Additionally, the absorption cross-section decreases by a factor of 3, reaching approximately 600 nm$^2$. The redshift pattern in the scattering cross-section is akin to that observed in the absorption cross-section, with a slight reduction up to the resonance wavelength followed by a maximum point. As nanoparticle radius increases, the size parameter grows, leading to multipolar resonant modes due to the heterogeneous distribution of free charges. Furthermore, an increase in the number of conduction electrons occurs due to the greater number of atoms.

When the radius of nanoparticles increases, several effects come into play. The larger volume leads to more atoms, resulting in an increased number of conduction electrons. However, due to limited electric field penetration, surface effects become prominent, leading to a heterogeneous distribution of free charges. Consequently, multipolar charge distributions emerge, causing higher scattering compared to absorption.

Similarly, we can find the extinction cross section as plotted in Fig. 3a to 3f.

Figure 4 clearly illustrates that scattering generally outweighs absorption at small nanoparticle radii. Consequently, in these cases, scattering dominates. As the nanoparticle radius increases, the absorption process gradually gains prominence, although scattering remains dominant. Notably, at longer wavelengths, absorption surpasses scattering, and larger nanoparticle radii enhance absorption. The Rayleigh approximation holds true within a 5 nm radius, resulting in

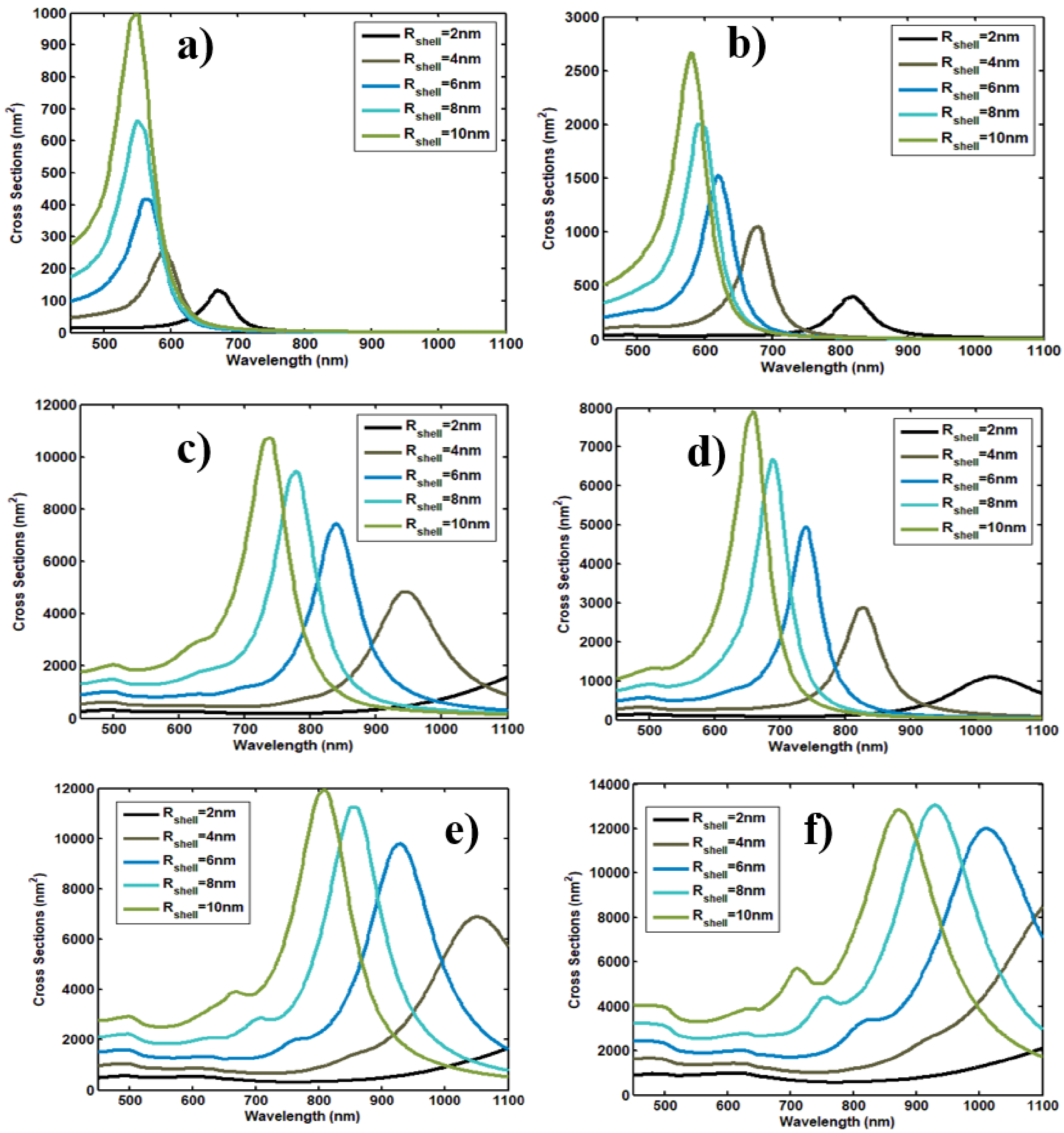


**Figure 1.** Absorption cross sections for nanoparticles with different core diameters (a) 5 nm, (b) 10 nm, (c) 20 nm, (d) 30 nm, (e) 40 nm (f) 50 nm.

single plasmon peaks arising from resonance in the bipolar distribution of free electrons within the nanoparticle. Specifically, the maximum extinction cross-section occurs for core diameters of 5 nm and shell diameters of 2, 4, 6, 8, and 10 nm, corresponding to wavelengths of 700, 630, 585, 570, and 560 nm, respectively. At radii significantly smaller than the incident wavelength, absorption remains significant compared to scattering, with a transition toward the blue peak in the cross-sections.

The Extinction cross-section is crucial because it accounts for both absorption and scattering effects. Analyzing how the extinction cross-section changes with varying nanoparticle radius provides valuable insights.

Increasing the Au shell thickness shifts the resonance toward longer wavelengths (redshift) and can reduce the absorption cross-section because the effective dielectric environment and conduction-electron distribution change; a thicker metallic shell increases the overall particle polarizability but also screens the core, altering the effective refractive index seen by surface plasmons. Conversely, a thinner shell allows stronger core–shell coupling and a resonance at shorter wavelengths. We also note that the surrounding dielectric (tissue or medium) further shifts and broadens the LSPR: higher refractive index environments produce

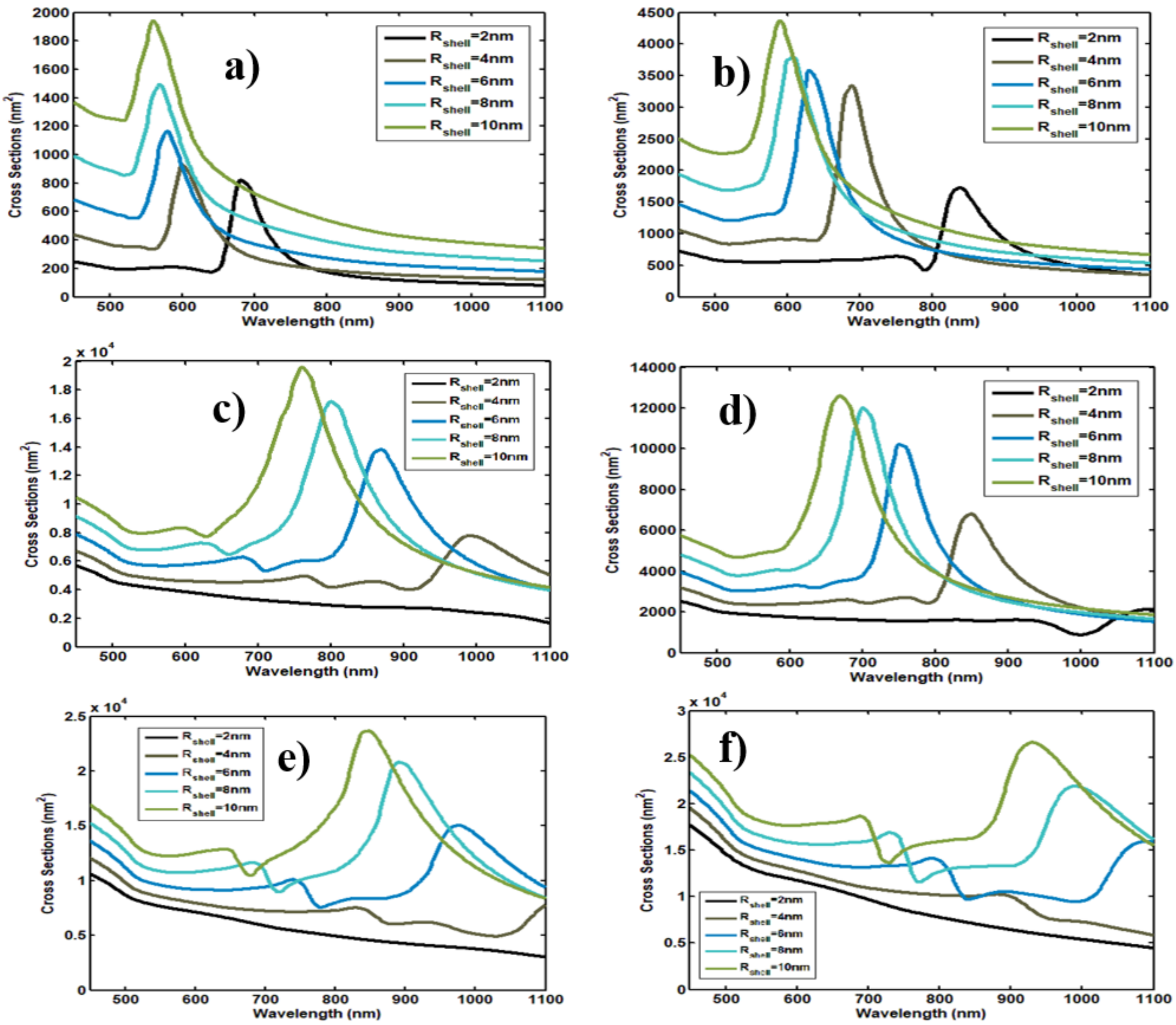


**Figure 2.** Scattering cross-sections for nanoparticles with different core diameters (a) 5 nm, (b) 10 nm, (c) 20 nm.

redshifts and increased damping.

In the subsequent step, we partition the tissue into two regions: one representing skin cancerous tissue and the other healthy tissue (as depicted in Fig. 5). Our goal is to irradiate laser light onto nanoparticles while ensuring that only the cancerous tissue's temperature increases, without harming the healthy tissue. For this simulation, we set the ambient temperature at 25 °C, the body temperature at 37 °C, and denote $T_0$ as 35 degrees Celsius. The relevant dimensions are outlined in Table 1. Additionally, we incorporate boundary conditions for heat transfer between the tissues and the environment, considering convective effects.

The incident laser has an intensity of 0.5 W/cm$^2$, a radius of 0.5 cm, and operates at a wavelength of 808 nm. In published articles, the duration of laser light irradiation on tissue varies due to factors such as tissue type, nanoparticle characteristics, and laser intensity [33–36]. For our simulation, we set the laser duration to 600 seconds, ensuring diffusion throughout the tumor area while minimizing leakage to healthy tissue. Figure 6a depicts temperature mapping on the tissue surface, highlighting changes at the tissue center and tumor center. Additionally, Fig. 6b displays isothermal lines within this structure.

When exposed to laser radiation, temperatures near the center of the tissue exceed those in surrounding areas. This temperature difference diminishes with increasing depth due to the laser's weakening heat penetration. The highest temperature occurs when the laser targets the tumor surface, specifically at the tissue center, where temperatures surpass 64 °C. As we move away from the laser point, the temperature decreases logarithmically. Notably, healthy tissue areas also experience temperatures exceeding 43 °C. While this effectively destroys the tumor, it unfortunately causes unintended damage to the surrounding healthy tissue.

To assess heat distribution at the radiation point, we examined temperature distribution along the $y$-direction at $x = 0$ and various depths. As depth increases, the temperature converges toward the initial temperature of healthy tissue (37 °C). Additionally, near the center of laser light radiation and the location of the desired shell-core nanoparticles, temperatures exceed those of the surrounding areas. The pseudo-Gaussian temperature profile in this direction arises

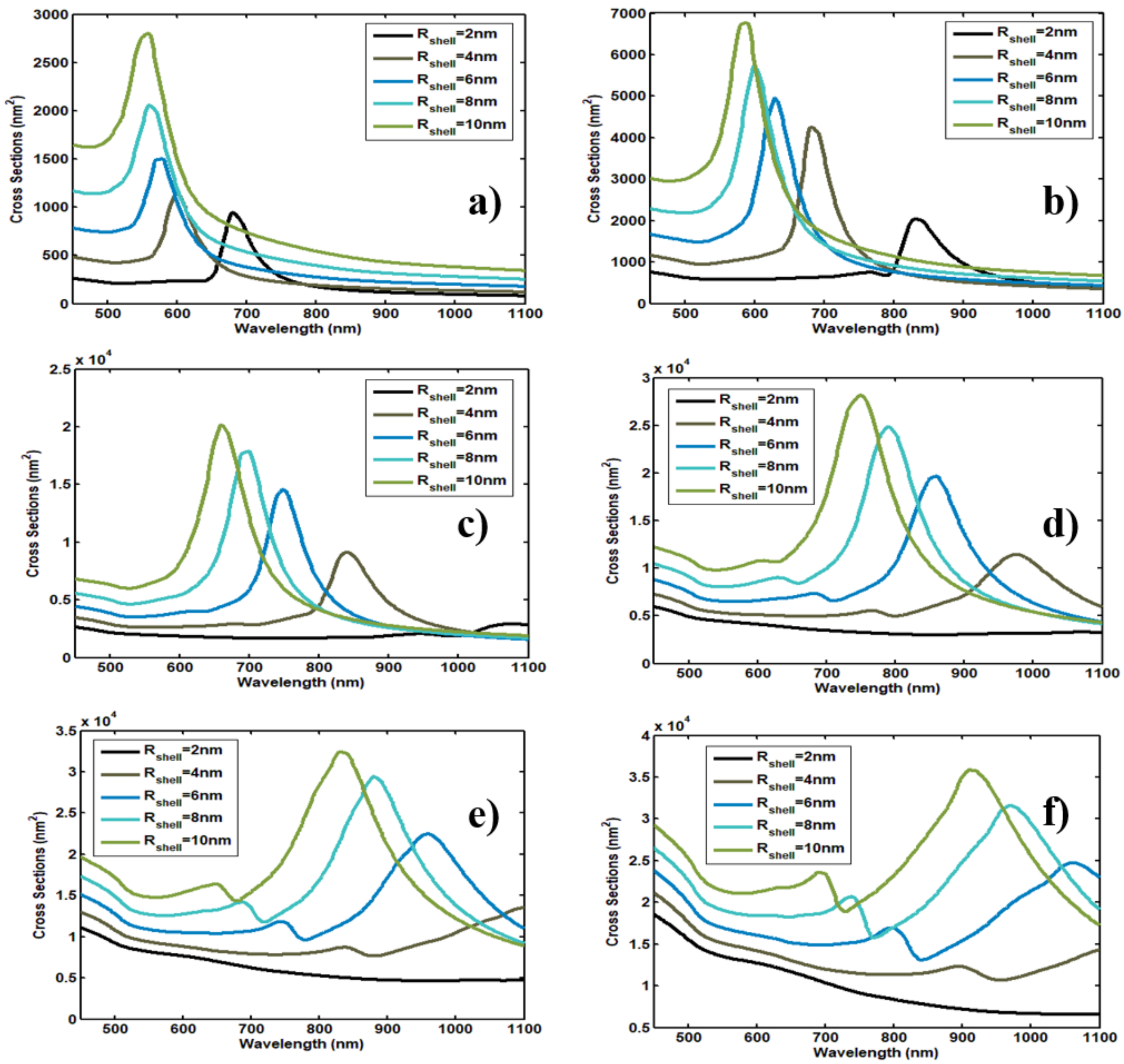


**Figure 3.** Extinction cross-section plots for nanoparticles with the core diameter (a) 5 nm, (b) 10 nm, (c) 20 nm, (d) 30 nm, (e) 40 nm, (f) 50 nm.

from the Gaussian nature of the laser in the transverse direction. Figure 7b displays temperatures at different points: Points A to D, adjacent to the tumor tissue, exhibit increased temperatures, while point $E$, representing healthy tissue, experiences a more modest temperature rise.

Figure 8 illustrates the tissue destruction mechanism. Notably, maximum destruction occurs at the desired level, corresponding to the laser's diameter. However, some cancer cells remain unaffected, necessitating adjustments to the laser radiation mechanism. Balancing temperature increase to destroy cancerous tissue while minimizing harm to healthy tissue remains a challenge.

## 4. Conclusion

In this study, we investigated the absorption and scattering cross-sections of magneto-plasmonic nanostructures ($Fe_3O_4$@Au) across various sizes and aspect ratios. Our results highlight the importance of selecting laser wavelengths based on core-shell dimensions for optimal hyperthermia outcomes. Additionally, we simulated local temperature distribution when $Fe_3O_4$@Au core-shells were placed in tumor tissue. Notably, the maximum tumor temperature reached 56 °C, while healthy tissue remained at 37 °C. These insights hold promise for effective hyperthermia treatment with minimal impact on surrounding healthy cells.

**Authors Contribution**
All authors have contributed equally to prepare the paper.

**Availability of data and materials**
The datasets generated during and/or analyzed during the current study are available from the corresponding author on reasonable request.

**Conflict of interests**
The authors declare that they have no known competing financial interests or personal relationships that could have appeared to influence the work reported in this paper.

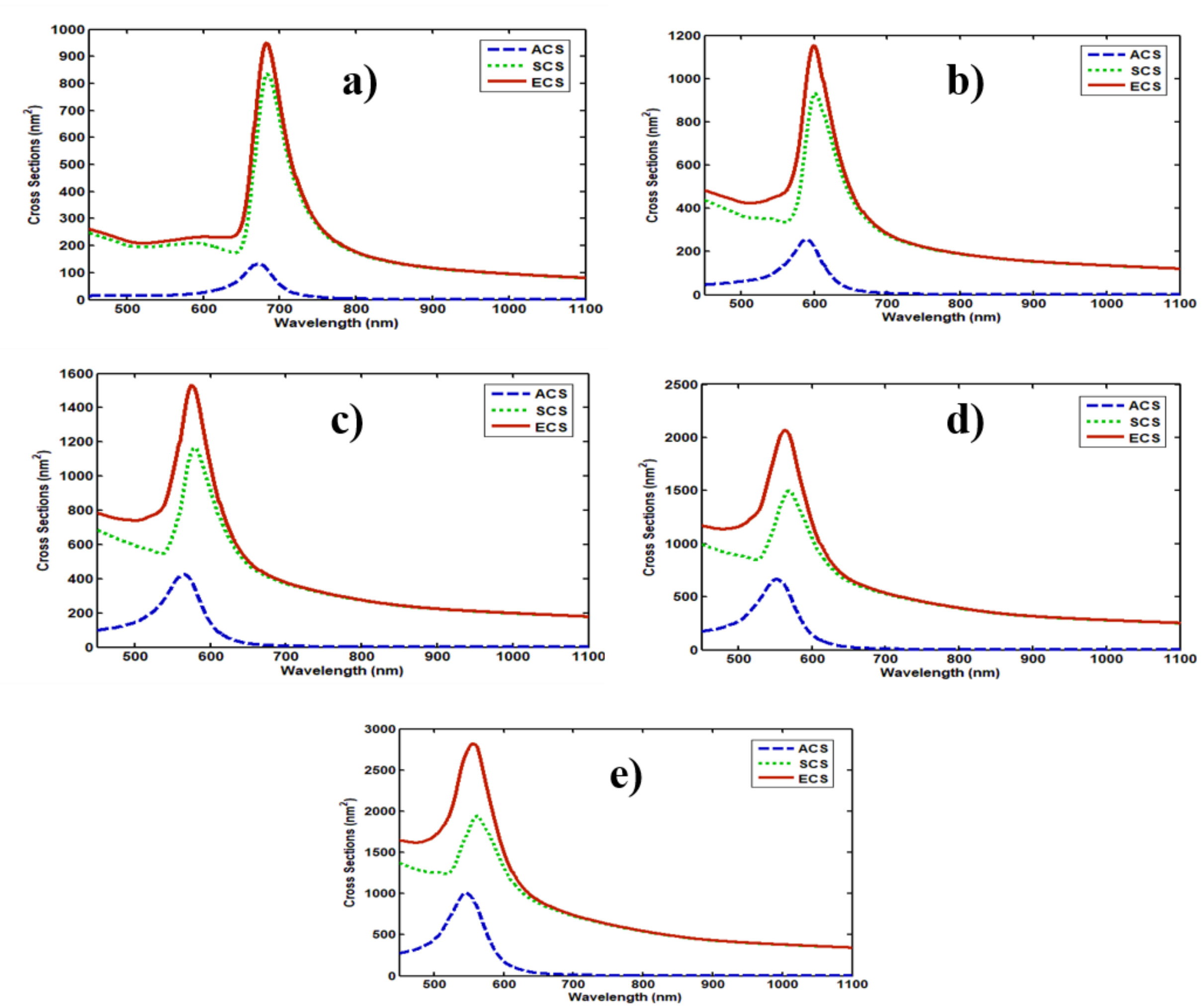


**Figure 4.** Absorption, scattering, and extinction cross-sections in core diameter of 5 nm and shell diameter (a) 2 nm, (b) 4 nm, (c) 6 nm, (d) 8 nm and (e) 10 nm.

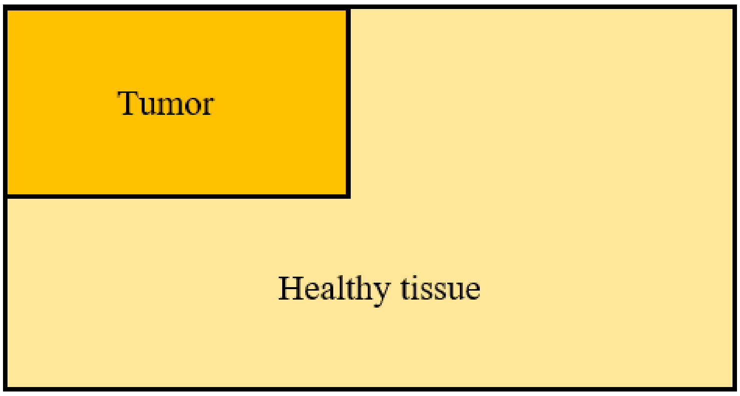


**Figure 5.** The schematic tumor and healthy tissues.

**Table 1.** The dimension of simulation.

| Name | Dimension (cm) |
|---|---|
| W_Tissue | 1 |
| H_Tissue | 0.6 |
| W_Tumor | 0.5 |
| H_Tumor | 0.3 |

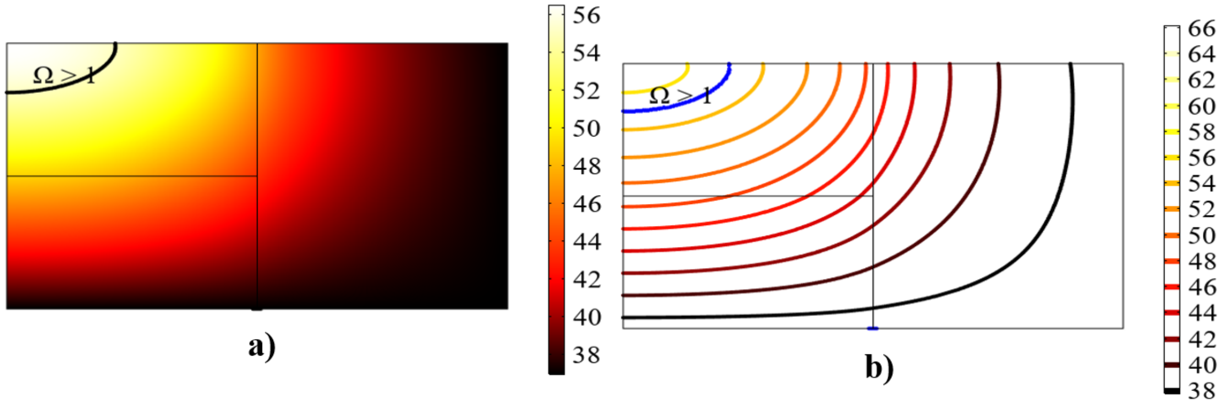


**Figure 6.** (a) The temperature in the form of mapping on the surface of the desired tissue (b) isothermal lines in this structure.

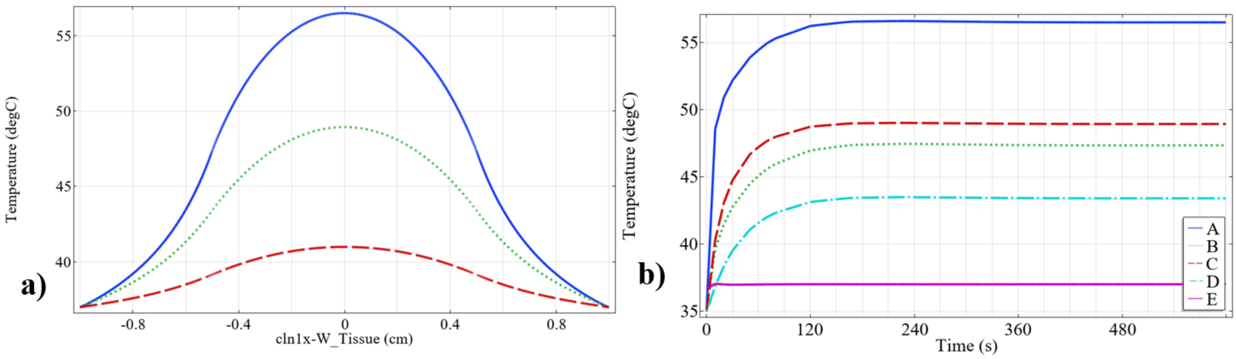


**Figure 7.** (a) Distribution of temperature in y direction at $x = 0$ (b) in different depth A to E.

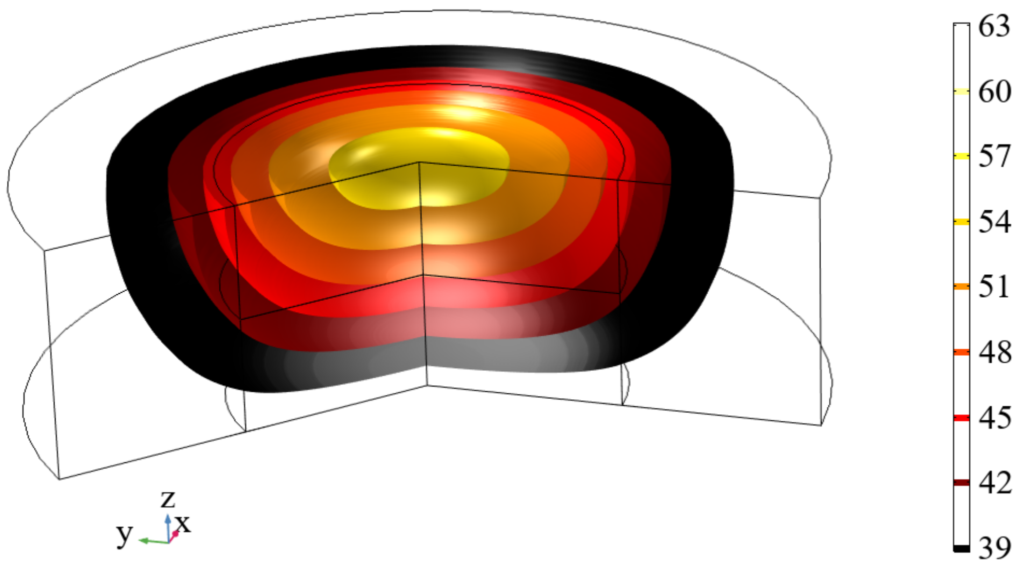


**Figure 8.** The destruction mechanism at the tissue level.

## References


[1] Kumar, S. S. R. Challa, and M. Faruq. Magnetic nanomaterials for hyperthermia-based therapy and controlled drug delivery. . *Advanced Drug Delivery Reviews*, **63**:789–808, (1996).
DOI: https://doi.org/10.1016/j.addr.2011.03.008.

[2] Rajan, Arunima, and N. Kumar Sahu. Review on magnetic nanoparticle-mediated hyperthermia for cancer therapy. . *Journal of Nanoparticle Research*, **22**:1–25, (2020).
DOI: https://doi.org/10.1007/s11051-020-05045-9.

[3] Ansah, I. Baffour, et al. In-situ fabrication of 3D interior hotspots templated with a protein@ Au core–shell structure for label-free and on-site SERS detection of viral diseases. . *Biosensors and Bioelectronics*, **220**:114930, (2023).
DOI: https://doi.org/10.1016/j.bios.2022.114930.

[4] A. Akouibaa et al. Optical and Dielectric Properties of Plasmonic Core–Shell Nanoparticles: $Fe_2O_3$/Au and $Fe_3O_4$/Au. . *Journal of Cluster Science*, :1–8, (2021).
DOI: https://doi.org/10.1007/s10876-021-02133-1.

[5] R. Yatao et al. Thermal dosage investigation for optimal temperature distribution in gold nanoparticle enhanced photothermal therapy. *International Journal of Heat and Mass Transfer*, **106**:212–221, (2017).
DOI: https://doi.org/10.1016/j.ijheatmasstransfer.2016.10.067.

[6] N. Osanloo et al. Analytical study of gold–DNA nano core–shell cloaking characteristics for drug delivery and cancer therapy. . *RSC Advances*, **13**:23244–23253, (2023).
DOI: https://doi.org/10.1039/D3RA03338D.

[7] O. Svinko Vasilisa et al. Comparative study of fluorescence core-shell nanotags with different morphology of gold core. . *Colloids and Surfaces B: Biointerfaces*, **226**:113306, (2023).
DOI: https://doi.org/10.1016/j.colsurfb.2023.113306.

[8] G. K. M. Hasanuzzaman, T. M. Sakib, and A. K. Paul. Gold coated surface plasmon resonance based biosensor: an hexagonal photonic crystal Fiber platform. . *Sensing and Bio-Sensing Research*, **42**: 100582, (2023).
DOI: https://doi.org/10.1016/j.sbsr.2023.100582.

[9] P. Tartaj et al. Advances in magnetic nanoparticles for biotechnology applications. *Journal of Magnetism and Magnetic Materials*, **290**: 28–34, (2005).
DOI: https://doi.org/10.1016/j.jmmm.2004.11.155.

[10] Mehmet V. Yigit, Anna Moore, and Zdravka Medarova. Magnetic nanoparticles for cancer diagnosis and therapy. *Pharmaceutical Research*, **29**:1180–1188, (2012).
DOI: https://doi.org/10.1007/s11095-012-0679-7.

[11] Bahareh Khaksar Jalali et al. Photothermal treatment of glioblastoma cells based on plasmonic nanoparticles. *Lasers in Medical Science*, **38**:122, (2023).
DOI: https://doi.org/10.1007/s10103-023-03783-5.

[12] David A. Garfinkel et al. Magnetic and Optical Properties of Au–Co Solid Solution and Phase-Separated Thin Films and Nanoparticles. *ACS Applied Materials & Interfaces*, **14**:15047–15058, (2022).
DOI: https://doi.org/10.1021/acsami.2c02028.

[13] Dheeraj Pratap et al. Photothermal properties of stable aggregates of gold nanorods. . *Colloids and Surfaces A: Physicochemical and Engineering Aspects*, **635**:128054, (2022).
DOI: https://doi.org/10.1016/j.colsurfa.2021.128054.

[14] Junyan Gong et al. High quality self-assembly magnetite ($Fe_3O_4$) chain-like core-shell nanowires with luminescence synthesized by a facile one-pot hydrothermal process. *Chemical Communications*, **46**: 3514–3516, (2010).
DOI: https://doi.org/10.1039/C002199G.

[15] Masoud Nejabat et al. An Overview on Gold Nanorods as Versatile Nanoparticles in Cancer Therapy. . *Journal of Controlled Release*, **354**:221–242, (2023).
DOI: https://doi.org/10.1016/j.jconrel.2023.01.009.

[16] M. H. Falk and R. D. Issels. Hyperthermia in oncology. *International Journal of Hyperthermia*, **17**:1–18, (2001).
DOI: https://doi.org/10.1080/02656730118511.

[17] van der Zee, Jacoba, et al. Comparison of radiotherapy alone with radiotherapy plus hyperthermia in locally advanced pelvic tumours: a prospective, randomised, multicentre trial. . *Lancet*, **355**:1119–1125, (2000).
DOI: https://doi.org/10.1016/S0140-6736(00)02059-6.

[18] Wenjie Yang et al. Gold nanoparticle based photothermal therapy: Development and application for effective cancer treatment. . *Sustainable Materials and Technologies*, **22**:e00109, (2019).
DOI: https://doi.org/10.1016/j.susmat.2019.e00109.

[19] Peter Wust et al. Hyperthermia in combined treatment of cancer. . *The lancet oncology*, **3**:487–497.

[20] Paula IP Soares et al. Application of hyperthermia for cancer treatment: recent patents review. . *Recent atents on anti-cancer drug discovery*, 7:64–73, (2012).
DOI: https://doi.org/10.2174/157489212798358038.

[21] Vienna E. Brunt et al. Passive heat therapy improves cutaneous microvascular function in sedentary humans via improved nitric oxide-dependent dilation. . *Journal of applied physiology*, **121**:716–723, (2016).
DOI: https://doi.org/10.1152/japplphysiol.00424.2016.

[22] Tomas. Drizdal et al. Hyperthermia treatment planning guided applicator selection for sub-superficial head and neck tumors heating. . *International Journal of Hyperthermia*, **34**:704–713, (2018).
DOI: https://doi.org/10.1080/02656736.2017.1383517.

[23] Y. Yamamoto, J. Ogasawara, H. Himukai, and T. Itoh. Effects of coating molecules on the magnetic heating properties of Au-$Fe_3O_4$ heterodimer nanoparticles. *Applied Physics Letters*, **109**(14), (2016).
DOI: https://doi.org/10.1063/1.4964514.

[24] Yang Liu et al. Rational synthesis and tailored optical and magnetic characteristics of $Fe_3O_4$–Au composite nanoparticles. *Journal of Materials Science*, **52**:10163–10174, (2017).
DOI: https://doi.org/10.1007/s10853-017-1200-9.

[25] Grace Brennan et al. Dark Field and Coherent Anti-Stokes Raman (DF-CARS) Imaging of Cell Uptake of Core-Shell, Magnetic-Plasmonic Nanoparticles. . *Nanomaterials*, **11**:685, (2021).
DOI: https://doi.org/10.3390/nano11030685.

[26] Fariborz Sharifianjazi et al. Biosensors and nanotechnology for cancer diagnosis (lung and bronchus, breast, prostate, and colon): A systematic review. . *Biomedical Materials*, **17**:012002, (2021).
DOI: https://doi.org/10.1088/1748-605X/ac41fd.

[27] Shaik Jakeer et al. Numerical and Machine Learning Approach for $Fe_3O_4$-Au/Blood Hybrid Nanofluid Flow in a Melting/Non-Melting Heat Transfer Surface with Entropy Generation. . *Symmetry*, **15**: 1503, (2023).
DOI: https://doi.org/10.3390/sym15081503.

[28] Hongdong Cai et al. Dendrimer-assisted formation of $Fe_3O_4$/Au nanocomposite particles for targeted dual mode CT/MR imaging of tumors. *Small*, **11**:4584–4593, (2015).
DOI: https://doi.org/10.1002/smll.201500856.

[29] Claus Feldmann. Preparation of nanoscale pigment particles. . *Advanced Materials*, **13**:1301–1303, (2001).
DOI: https://doi.org/10.1002/1521-4095(200109)13:17¡1301::AID-ADMA1301¿3.0.CO;2-6.

[30] Nardine S. Abadeer and Catherine J. Murphy. Recent Progress in Cancer Thermal Therapy Using Gold Nanoparticles. . *J. Phys. Chem. C*, **120**:4691–4716, (2016).
DOI: https://doi.org/10.1021/acs.jpcc.5b11232.

[31] Sikdar, Debabrata, Wenlong Cheng, and Malin Premaratne. Optically resonant magneto-electric cubic nanoantennas for ultra-directional light scattering. . *Journal of Applied Physics*, **117**, (2015).
DOI: https://doi.org/10.1063/1.4907536.

[32] Charny and Caleb K. Mathematical models of bioheat transfer. *Advances in heat transfer*, **22**:19–155, (1992).
DOI: https://doi.org/10.1016/S0065-2717(08)70344-7.

[33] Muhammad Usama Daud et al. Finite element analysis of silver nanorods, spheres, ellipsoids and core–shell structures for hyperthermia treatment of cancer. . *Materials*, **15**:1786, (2022).
DOI: https://doi.org/10.3390/ma15051786.

[34] Faruq Mohammad et al. Magnetically controlled drug delivery and hyperthermia effects of core-shell Cu@$Mn_3O_4$ nanoparticles towards cancer cells in vitro. *International Journal of Biological Macromolecules*, **249**:126071, (2023).
DOI: https://doi.org/10.1016/j.ijbiomac.2023.126071.

[35] Sandeep B. Somvanshi et al. Core-shell structured superparamagnetic Zn-Mg ferrite nanoparticles for magnetic hyperthermia applications. . *Journal of Alloys and Compounds*, **947**:169574, (2023).
DOI: https://doi.org/10.1016/j.jallcom.2023.169574.

[36] Dnyaneshwar Kalyane et al. Recent advancements and future submissions of silica core-shell nanoparticles. *International Journal of Pharmaceutics*, **609**:121173, (2021).
DOI: https://doi.org/10.1016/j.ijpharm.2021.121173.